Journal of Materials Chemistry A

ROYAL SOCIETY OF CHEMISTRY

PAPER

View Article Online
View Journal | View Issue

Cite this: J. Mater. Chem. A, 2025, 13, 31699

Redox-active biomineralised zeolitic imidazolate frameworks enable peroxidase bioelectrocatalysis with shielding against substrate inhibition and thermal inactivation

Monika Joharian,[a] Alexandre Uzel,[b] Abir Elloumi,[ac] Yannig Nedellec,[a] Thierry Encinas,[d] Serge Gambarelli[b] and Andrew J. Gross *[a]

Oxidoreductase enzymes have remarkable advantages in terms of activity and selectivity but their fragility and buried active sites hinder their practical use for bioelectrochemical applications. Solutions are required to address the limited stability of enzyme-electrode interfaces while permitting efficient electron transfer, especially under harsh inhibiting and deactivating conditions. Inspired by natural biomineralisation, we developed a protected redox-active biomineralised peroxidase/zeolitic imidazolate framework electrode in which the fragile enzyme is electrically-accessible and shielded from substrate inhibition and thermal deactivation. In contrast to previous biomimetic metal organic frameworks developed for biocatalysis, the biomineralised frameworks reported here comprised enzyme together with a benzothiazoline redox mediator to enable electron shuttling across and/or from the crystalline matrix. Both redox entities proved necessary to overcome the insulating zeolitic framework barrier. This strategy provided benefits such as 3-fold enhanced bioelectrocatalytic currents and remarkable protection at high inhibitor (peroxide) concentrations of *ca.* 0.5–5 mmol L^{-1} up to 50 °C. The protective framework offered improved 1-week storage stability and permitted biosensor linear range expansion from 0.1 to 0.5 mmol L^{-1}. Limitations were observed in terms of sensor sensitivity and high temperature deactivation. Redox-active biomineralised MOFs hold promise for extending bioelectrocatalytic outputs under harsh conditions for future biosensors, biofuel cells and bioreactors.

Received 7th April 2025
Accepted 13th August 2025

DOI: 10.1039/d5ta02717a

rsc.li/materials-a

Introduction

Enzymes are nature's remarkable catalysts that accelerate biochemical reactions with high selectivity and efficiency, but they are complex and fragile. The electrical wiring of oxidoreductase enzymes at electrodes offers the possibility to combine the advantages of biocatalysis with electrocatalysis.[1,2] In recent years, the integration of enzymatic electrodes into implantable and wearable devices has attracted considerable interest for biosensing and energy harvesting biofuel cells towards a healthier and more sustainable future.[3–9] Portable and wearable glucose monitors that employ bioelectrodes with immobilised flavin-adenine dinucleotide (FAD)-dependent glucose enzymes such as glucose oxidase (GOx) have revolutionised the treatment and management of diabetes.[7,10] Commercial lactate, ketone and alcohol monitors are anticipated but the enzyme-electrode interfaces lack robustness.[11] The coupling of enzymes with electrodes also offers promise for the electrosynthesis of value-added chemicals with regio-, chemo-, and enantio-selectivity, but such bioreactors are also limited by enzyme fragility.[12,13] The development of enzymatic electrodes for practical applications beyond glucose biosensors and fragile biofuel cells is highly desirable but extremely challenging. The limited stability of enzymatic electrodes is a major technological bottleneck owing to the intrinsic fragility of enzymes and the limited interfacial robustness of enzyme-electrode interfaces. Obtaining effective electron transfer and mass transport at enzymatic electrodes is also challenging due to factors such as (i) the distance between the electrode and the often deeply-buried active redox site of the enzyme, (ii) enzyme orientation with respect to the electrode surface, (iii) electrode porosity, (iv) the nature of the charge transfer pathway, and (v) the potential and activity of the redox mediator employed, where redox mediators are commonly required to enable bioelectrocatalysis.[14]

Substrate inhibition, also known as "suicide inactivation", is a common type of enzyme inactivation that reportedly affects *ca.* 25% of enzymes.[15] The loss in activity results from the binding

[a]Department of Molecular Chemistry, UMR CNRS-UGA 5250, Université Grenoble Alpes, 38000 Grenoble, France. E-mail: andrew.gross@univ-grenoble-alpes.fr
[b]Univ. Grenoble Alpes, CNRS, CEA, IRIG, SyMMES, Grenoble, 38000, France
[c]Laboratory of Interfaces and Advanced Materials, Faculty of Sciences, University of Monastir, 5019 Monastir, Tunisia
[d]CMTC, Grenoble Institute of Technology, 38000 Grenoble, France

of the substrate inhibitor to the enzyme and/or the enzyme-substrate complex. Oxidoreductases including hemoproteins such as peroxidases, and flavoproteins such as lactate oxidase (LOx), are affected by substrate inhibition.[16,17] Such inhibition can impact H_2O_2 and lactate biosensors with respect to catalytic current (signal) magnitude, robustness, sensitivity, and detection range.[18–20] Substrate inhibition is also a limitation for certain enzymes for biofuel cell and bioreactor applications where high substrate concentrations are used to boost power and product formation outputs, respectively.[21,22]

Peroxidases are heme-Fe^{III} porphyrin proteins that catalyse oxidative reactions with peroxides such as H_2O_2 as the substrate. Over the past 30 or so years, peroxidase-based electrochemical sensors, most commonly employing horseradish peroxidase (HRP; EC 1.11.1.7), have been widely reported for the detection of peroxide, phenols and toxic compounds.[19,23,24] HRP is widely available and, in contrast to many enzymes, capable of both direct and mediated electron transfer (DET, MET) bioelectrocatalysis. At carbon electrodes such as graphite and carbon nanotubes, the bioelectrochemical reduction reaction selectively converts H_2O_2 to H_2O.[17,24,25] In biofuel cells, HRP has been used at biocathodes to drive H_2O_2 conversion, or to remove parasitic peroxide generated *in situ* at bioanodes.[26–28] Carbon-based HRP biocathodes can deliver high onset potentials of *ca.* 0.6 V at pH 7 (*vs.* Ag/AgCl). They can also avoid the stability limitations of benchmark O_2-reducing multicopper oxidase biocathodes that are inhibited by ions such as chloride or urate.[27] Unlike O_2-reducing biocathodes, HRP biocathodes can operate in anoxic environments and are not limited by low substrate solubility (*ca.* 1.1 mmol L^{-1} for dioxygen).[28,29] The substrate inhibition mechanism for HRP is widely considered to occur *via* a complex process involving the conversion of the native Fe^{III}-porphyrin to an oxo-Fe^{IV} pi-cation radical heme that, at high peroxide levels, leads to the formation of oxyperoxidase (peroxy-Fe^{III} porphyrin free radical or "compound III") that inhibits the catalytic activity.[17,30,31] There are several possible decomposition pathways and side reactions, including the formation of catalytically inactive verdohemoprotein (designated as P670) *via* irreversible reactions.[30,32]

Recent advances to improve the stability of enzymes and enzyme-electrode interfaces rely on polymer crosslinking to fix and/or encapsulate biocatalytic elements at the electrode. Zwitterionic biocompatible coatings offered improved glucose biosensor stability to the foreign body response compared to conventional polymer coatings based on poly(ethylene glycol).[33] Crosslinked dextran-methacrylate biopolymer coatings and redox-poly(ethylene glycol) polymers provided improvements in glucose biosensor operational and storage stability.[4,34] In pioneering works, Plumeré and coworkers developed redox polymers or "shields" to protect fragile enzymes from specific O_2 inactivation.[35,36] Beloqui, Conzuelo and workers very recently demonstrated an original polymer-biomineralisation strategy in which enzyme was protected in a Co-phosphate polymer-mineral matrix.[37] A proof-of-concept glucose biosensor and enhanced biocatalytic thermostability and solvent resistance were demonstrated.[37] This hybrid material approach nevertheless presents complexity due to the need to synthesise polymer-enzyme gels prior to the biomineralisation process. Despite the promise of such stabilisation systems, there is still a clear need for solutions to mitigate enzyme fragility and improve the robustness of enzyme-electrode interfaces under challenging conditions for practical bioelectronics devices.

Biomineralised metal organic frameworks (MOFs) based on zeolitic imidazolate frameworks (ZIFs) have provided unprecedented protection to encapsulated proteins for biocatalysis under denaturating conditions (*i.e.* organic solvents, high temperatures).[38] Biomimetic mineralisation is a type of "*de novo* encapsulation" referring to the strategy of combining MOF precursors together with enzyme (or microbes) to assemble MOFs *in situ* around the biomacromolecules, to infer protection such as shielding against enzyme unfolding.[39,40] Enzyme@-MOFs comprising enzymes such as glucose oxidase or HRP can maintain high activity when the encapsulation process involves enzyme-driven nucleation or facilitated nucleation *e.g.* with polyvinylpyrrolidone/cysteine.[38,41,42] Crystalline porous MOFs provided suitable substrate/product mass transport for biocatalysis, but it remains unclear if they can be used practically for bioelectrocatalysis due to their stability and electron transfer limitations. A biomineralised Zn-based azolate MOF with embedded GOx and HRP enzymes, GOx/HRP@MAF-7, was previously reported in the context of bioelectrocatalysis for biofuel cells.[43] The protective effects for biocatalysis were demonstrated but the electro-oxidative process and evidence for enzyme-electrode electron transfer are unclear.[43] MOFs and MOF-polymer systems have been used as materials in a few other examples but, to our knowledge, not 'pristine' biomimetic mineralised MOFs.[44] Solvothermal mesoporous MOFs, that are unsuitable for *in situ* enzyme encapsulation, were used as porous supports for immobilising and protecting enzymes.[45] The HRP enzyme (*ca.* 4–6 nm size) was encapsulated in an Fe-based MOF, PCN-333(Fe), and after coating with Nafion, explored for bioelectrocatalytic H_2O_2 sensing, with a redox mediator added in solution. The specific benefits due to MOF encapsulation of the enzyme are not clear; the benefits may be related to MOF collapse and/or the Nafion polymer employed.[45] The observed loss in the Brunauer–Emmett–Teller (BET) surface area after enzyme incorporation may indicate collapse of the crystalline MOF structure, in line with studies that highlight significant MOF degradation in aqueous/buffer solutions.[44] Very recently, Tsujimura and coworkers reported a breakthrough in the development of MOFs for bioelectrochemistry.[46] A redox-active "mediator" MOF was obtained by partial ligand substitution of a zeolitic imidazolate MOF, ZIF-67, then immobilised at a carbon electrode and employed as a redox mediator layer.[46] Well-defined mediated electron transfer bioelectrocatalysis was demonstrated. Stable continuous monitoring of glucose and lactate (54 h and 8 h, respectively) were also observed, benefitting from the hybrid MOF-hydrogel system employing crosslinked chitosan–genipin. The LOx bioelectrode suffered from bioelectrode deactivation, for example, due to substrate and/or product enzyme inhibition or deactivation. Furthermore, the latter ZIF-67 materials were not designed as an architecture to encapsulate and protect fragile enzymes.

Here, we further extend the development of biomimetic MOFs for biocatalysis to a strategy designed to enable effective electron shuttling between biomineralised enzyme and a nanostructured electrode, to protect the enzyme and drive bioelectrocatalysis. To the best of our knowledge, no such redox mediator/enzyme biomimetic system has been developed for bioelectrocatalysis. We move away from the classical approach of using polymer chemistry and crosslinkers, and their use to boost 'general' stability performance, to a strategy that focusses on (i) a simple and economical mineralisation process, and (ii) protecting enzymes from specific deactivation processes (*e.g.* substrate inhibition). Herein, a series of crystalline mineralised ZIF materials were synthesised, characterised and explored as new redox-active materials for bioelectrocatalysis with protection against enzyme inhibition and thermal deactivation. HRP was chosen as a versatile model oxidoreductase, capable of both direct and mediated electron transfer bioelectrocatalyis. The overall goal is to push enzymatic electrodes towards practical bioelectrochemical devices capable of operating under harsh conditions. As well as new insight into ZIF biomineralisation, enzyme inhibition, and thermal deactivation, and the development of new protective materials for bioelectrocatalysis, this study demonstrates a promising proof-of-concept peroxide biosensor.

Results and discussion

Synthesis, characterisation and biocatalysis of redox-active (bio)mineralised ZIF-8

The redox-active mineralised and biomineralised ZIF-8, as well as classical ZIF-8, were all synthesised *via* self-assembly of the organic linker, 2-methylimidazole (2-MeIm), and the metal salt (Zn nitrate) in deionised (DI) water at room temperature (RT). The redox-active mineralised ZIF-8 was obtained by assembly in the presence of a water-soluble artificial redox mediator, 2,2′-azino-bis(3-ethylbenzthiazoline-6-sulfonic acid) (ABTS). The redox-active biomineralised ZIF-8 materials were synthesised in the presence of HRP and either in the presence or absence of ABTS. These materials are herein designated as ABTS@ZIF-8, HRP@ZIF-8, and ABTS/HRP@ZIF-8. Falcaro and coworkers reported the biomineralisation of HRP@ZIF-8 with a 1 : 4 metal : ligand molar ratio.[38] The authors showed that the biomineralisation process forms a porous and crystalline ZIF-8 that embedded enzymes with a nanometric crystalline outer shell. To further promote the formation of crystalline rather than amorphous ZIFs, we employed a high metal:ligand ratio of 1 : 160. According to a previous study, higher metal:ligand ratios promote the nucleation and crystal growth of enzyme@ZIF-8 materials.[47] Enzyme@ZIF-8 materials notably followed the oppose trend to classical ZIF-8. In the latter case, the crystallite size increased with decreasing metal:ligand ratio from 1 : 100 to 1 : 20, for aqueous ZIF-8 synthesis with Zn nitrate as the metal precursor.[48] Tong and coworkers provided atomic-level insight into enzyme@ZIF-8 materials, revealing the crucial importance of crystallisation pathways on mass transport and biocatalysis.[49] Following the initial 30 min reaction, we employed an overnight stationary aging protocol. The stationary aging protocol, considered as the "stationary crystallisation phase" was used to target the transformation of initially amorphous halos into more homogeneous crystalline materials.[47]

Fig. 1A illustrates the biomineralised redox MOF concept designed to offer protection to a nanostructured bioelectrode for the 2-electron 2-proton bioelectrocatalytic reduction of H_2O_2 to water. The concept involves a nanostructured bioelectrode comprising multiwalled carbon nanotubes (CNTs) with an immobilised layer of redox-active ABTS/HRP@ZIF-8. We emphasise that no polymers or hydrogels were employed to enhance stability of electron transfer, thus permitting a clear evaluation of the role of the MOF for bioelectrocatalysis. The MOF-modified bioelectrode was then used for the bioelectrocatalytic H_2O_2 reduction reaction to H_2O with protection against substrate (H_2O_2) inhibition. ABTS was employed as a well-known redox mediator (electron relay) for the HRP enzyme. ABTS benefits from a chemically reversible single electron transfer process involving the formation of cationic radicals stabilised through resonance.[50,51] ABTS possesses sulfonic acid functional groups that promote its water solubility, hence it was an attractive choice for aqueous ZIF-8 biomineralisation synthesis. For clarity, the bioelectrocatalytic reaction shown in Fig. 1A involves electron percolation between the enzyme and the electrode to drive H_2O_2 reduction with the generation of a corresponding electrochemical signal measured either by voltammetry or amperometry. This catalytic current signal forms the basis of the inhibition study and electrochemical peroxide biosensor described later in the manuscript.

The possibility to obtain the ABTS/HRP@ZIF-8 material with both enzyme and redox mediator cargo *via* the high metal:ligand ratio method was first confirmed by scanning electron microscopy (SEM) and powder X-ray diffraction (pXRD). The SEM analysis of ABTS/HRP@ZIF-8 revealed the formation of distinct and rough spherical nanoparticles with an average diameter of $D = 148 \pm 43$ nm (Fig. 1B, S1 and S2). In contrast, larger well-defined rhombic dodecahedral with truncated edge morphologies were observed for HRP@ZIF-8 ($D = 504 \pm 178$ nm) and ZIF-8 ($D = 401 \pm 125$ nm). The ABTS@ZIF-8 nanoparticles ($D = 308 \pm 87$ nm) exhibited a smaller and more monodisperse hybrid spherical morphology with less well-defined crystalline facets. The smaller particle sizes and loss in crystal facets for ABTS@ZIF-8 and ABTS/HRP@ZIF-8 highlight a strong influence of the ABTS that partially disrupts MOF crystallisation *i.e.* Zn^{2+} coordination to the 2-MeIm ligand to form the characterstic Zn–N bonds. The disruption may be due to competition between the 2-MeIm ligand and the anionic sulfonic acid groups for Zn^{2+}.

The observed biomineralised morphologies contrast to the larger flower-like μm-sized particles of biocatalytic HRP@ZIF-8 reported previously, reflecting the different synthetic protocols and the effect of factors such as metal:ligand ratio, precursor concentrations, and redox cargo.[38,52] The pXRD patterns in Fig. 1C confirm the crystalline nature of the synthesised biomineralised materials. The materials correspond to classical ZIF-8 with sodalite (SOD) topology, irrespective of the presence of the redox enzyme and/or ABTS redox mediator during synthesis. The pXRD pattern for mineralised ABTS@ZIF-8 is

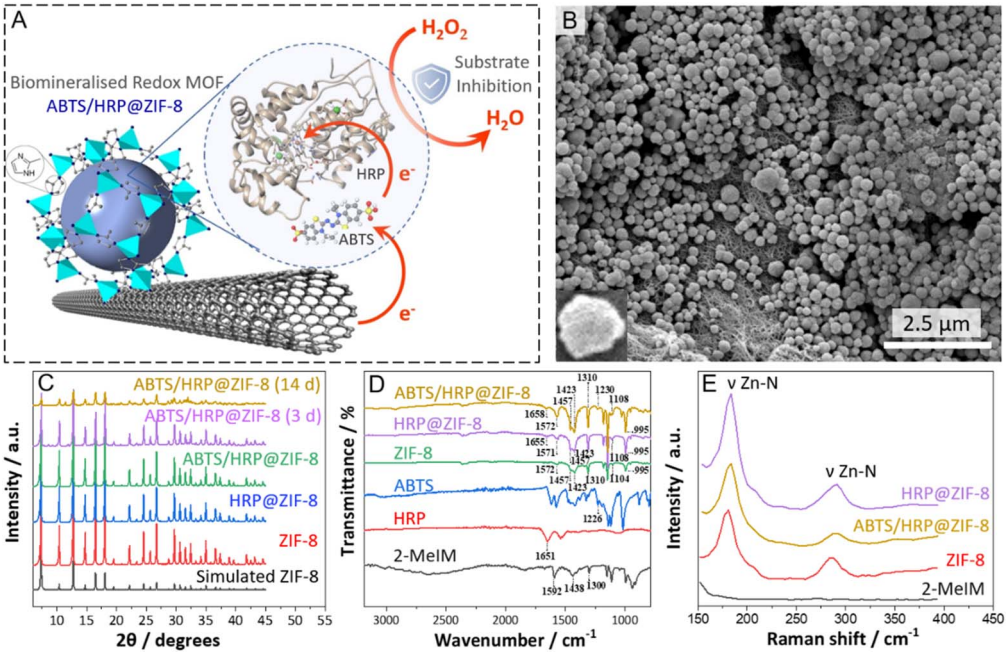

Fig. 1 (A) Scheme illustrating the mediator/enzyme redox MOF concept for bioelectrocatalytic H_2O_2 reduction with substrate inhibition protection *via* redox-active ABTS/HRP@ZIF-8 at a nanostructured CNTs electrode. (B) SEM micrograph of ABTS/HRP@ZIF-8 at CNTs (10 000× magnification). (C) pXRD diffractograms recorded at powders: (black) literature ZIF-8, (red) as-synthesised ZIF-8, (blue) HRP@ZIF-8, (green) ABTS/HRP@ZIF-8, and (purple, bronze) aged ABTS/HRP@ZIF-8 after immersion in 50 mmol L^{-1} phosphate buffer (PB) pH 7 for (purple) 3 days and (bronze) 14 days. (D) FT-IR spectra on powders of (black) 2-MeIm, (red) HRP, (blue) ABTS, (green) ZIF-8, (purple) HRP@ZIF-8, and (bronze) ABTS/HRP@ZIF-8. (E) Raman spectra on powders of (black) 2-MeIm, (red) ZIF-8, (purple) HRP@ZIF-8, and (bronze) ABTS/HRP@ZIF-8. The simulated pattern of sod-ZIF-8 is from the CIF file: 4118891.

available in Fig. S3. The formation of crystalline materials is in contrast to the amorphous ZIF (aZIF) structures obtained with single/multi-enzyme cargo *via* synthesis at low metal:ligand ratios and/or with minimal stationary aging.[47,53,54] The materials synthesised here did not exhibit broad diffraction peaks at high 2θ values of 20–40°. Such broad peaks are characteristic behaviour for highly amorphous material (*e.g.* protein-induced amorphous solid).[54] The stability of the crystalline samples to long term immersion in a physiological buffer, 50 mmol L^{-1} phosphate buffer (PB) pH 7, was confirmed by pXRD (Fig. 1C) with complimentary SEM (Fig. S1) measurements. The diffraction patterns are largely maintained after 3 days and 14 days for the ABTS/HRP@ZIF-8, consistent with resistance to phosphate buffer degradation over a practical timeframe for bioelectrochemical applications. Nevertheless, while significant crystallinity preservation is observed, peak broadening, signal loss, and new reflections reveal structural ZIF-8 degradation and the presence of impurities.[55] Complimentary SEM data (Fig. S1) shows that the rough spherical nanoparticle morphologies remain largely intact after 50 mmol L^{-1} pH 7 phosphate buffer immersion for 3 days and 14 days.

Fourier transform infrared spectroscopy (FT-IR) and Raman spectroscopy were used to probe the chemical nature of the ABTS/HRP@ZIF-8 and related ZIF materials. Both techniques yielded spectra consistent with reported crystalline ZIF-8 and HRP@ZIF-8 (Fig. 1D and E, S4 and S5). The FT-IR bands at 1655 cm^{-1} and 1658 cm^{-1}, characteristic of the amide I band (C–O, stretch), confirm the presence of protein in the HRP@ZIF-8 and ABTS/HRP@ZIF-8 MOFs. A small shift of the amide I band compared to HRP only (1651 cm^{-1}) was observed. Small shifts have previously been attributed to direct protein-MOF interactions between carbonyl groups of the protein backbone and Zn^{2+} defect sites, as reported for BSA@ZIF-8.[38] The peaks at 1230 cm^{-1}, attributed to sulfonic acid groups (S–O, stretch), confirm the successful encapsulation of the mediator in the ABTS@ZIF-8 and ABTS/HRP@ZIF-8 materials (Fig. 1D and S4). The slight red shift compared to ABTS (1226 cm^{-1}) may be evidence for sulfonic acid binding with Zn^{2+} ions and/or interactions with the enzyme, which could eventually be linked to differences in enzyme activity and stabilisation. The FT-IR vibrational modes overall confirm defective as opposed to pristine crystalline ZIF-8 materials.[56] The broad feature at *ca.* 1110 cm^{-1} (C–N–H, C–H) with peaks at 1560–1580 cm^{-1} (C–N–H) is interpreted as being characteristic of missing Zn defects and/or the presence of entrapped species (2-MeIm, ABTS, HRP). The modes at 1420–1460 cm^{-1}, *ca.* 1310 cm^{-1}, and 995 cm^{-1}, may be attributed to ZIF-8 C–H methyl and ring vibrations.[56] The Raman spectra (Fig. 1E and S5) show strong peaks at *ca.* 177–184 cm^{-1} and 284–291 cm^{-1} for the ZIF-8 materials, corresponding to the Zn–N stretching vibrations of the coordination structure.[57] The slight shifts in peak position may reflect changes in the Zn coordination structure but this was not probed further.

To confirm the presence of active enzyme in ABTS/HRP@ZIF-8, a classical UV-vis spectroscopy activity assay was performed. For the biocatalytic assay, a solution of ABTS then H_2O_2 were

added into a cuvette containing either HRP or the biomineralised ZIF-8 in 50 mmol L^{-1} PB pH 7. Relative activities were determined by monitoring the absorbance of this mixture at $\lambda = 418$ nm, where the absorbance corresponds to the enzymatically generated $ABTS^{\bullet+}$ radical cation formed during H_2O_2 reduction to H_2O. As shown in Fig. 2A, the initial reaction rates were similar for ABTS/HRP@ZIF-8 compared to the free HRP across the temperature range studied of 25 °C to 50 °C, within the limits of experimental error. Pertinently, the porous crystalline redox ZIF-8 structure not only allows effective mass transport of reactant/product, but it permits a high level of activity to be maintained under conditions of low, non-inhibiting peroxide concentration (80 μmol L^{-1}). MOF encapsulation of enzymes generally leads to compromised activity under mild conditions *e.g.* due to decreased enzyme flexibility and mass transport, although some literature has shown increased activities, attributed to limited structural rearrangements and the prevention of aggregation.[58,59]

Low-temperature electron paramagnetic resonance (EPR) experiments were also performed in both the solid state and the solution state (10 mmol L^{-1} PB pH 7) that, importantly, confirmed the presence of the intact heme active site in the ABTS/HRP@ZIF-8 composite (Fig. S6). The EPR spectra of ABTS/HRP@ZIF-8 in the solid state and in the phosphate buffer solution are very similar to those of ABTS@ZIF-8, except for additional lines observed at effective $g \approx 6.39$ and 5.91, attributed to HRP embedded in the MOF. The shape and effective g values are somewhat different to those obtained for pure HRP in the buffer, reflecting the enzyme's sensitivity to confinement in the local MOF microenvironment. It is well known that the pH and chemical nature of the buffer can have strong effects on these EPR signals.[60] The spectra obtained for HRP in the solid state and in the buffer are similar to those found in the literature with characteristic signals with effective $g \approx 6.39$, 4.98, 1.98.[61] EPR experiments were also performed to test the reactivity with H_2O_2 (Fig. S7). After reaction with 3 mmol L^{-1} H_2O_2 for ≈30 s in 10 mmol L^{-1} PB pH 7, a complete loss of the EPR lines at effective $g \approx 6.39$, 4.98, and 1.98 at HRP alone was observed, consistent with conversion to a catalytic intermediate and/or inhibited HRP. In contrast, for ABTS/HRP@MOF, this conversion was not completed since these lines did not disappear. It is not clear if the differences are related to mass transport or intrinsic enzyme reactivity; nevertheless, the experimental evidence is consistent with enzyme confinement in the MOF.

The permanent porosity of ABTS/HRP@ZIF-8, HRP@ZIF-8 and ZIF-8 samples was examined by N_2 sorption analysis at 77 K (Fig. 2B and C). The isotherms display the general profile of a type I isotherm, signaling their microporous nature, with a high adsorption capacity at very low relative pressures (Fig. 2B). This is consistent with previous ZIF-8 and biomineralised enzyme@ZIF-8 composites.[38] BET analysis revealed smaller surface areas of 1386 and 1428 $m^2\ g^{-1}$ for ABTS/HRP@ZIF-8 and HRP@ZIF-8 compared to 1534 $m^2\ g^{-1}$ for ZIF-8. The decrease in surface area for the biomineralised MOFs compared to pristine ZIF-8 is consistent with blocking of some micropores with encapsulated enzyme/mediator. The micropore distribution according to the Horvath–Kawazoe method, shown in Fig. 2B, revealed similar size distributions at ∼0.8 nm, ∼1.1 nm, and ∼1.3 to 1.4 nm. No obvious trend relating pore size to guest species encapsulation could be observed.

The enzyme and mediator loading amounts in the redox ZIF materials were determined by UV-vis spectroscopy according to calibration curves (Fig. S8 and S9). The loading amounts were calculated by subtracting the concentrations determined in the supernatant solutions after washing and high-speed centrifugation (12 000 rpm) steps. The enzyme concentrations were determined from the Soret adsorption band ($\lambda = 402$ nm) of the heme prosthetic group of the enzyme, as shown in Fig. S8. The characteristic absorption of ABTS in the reduced state ($\lambda = 339$ nm) was used for ABTS quantification.[51] Enzyme and redox mediator encapsulation efficiencies were obtained from the final and initial mass loading amounts. The estimated loading amounts and encapsulation efficiencies for HRP@ZIF-8, ABTS@ZIF-8, and the ABTS/HRP@ZIF-8 materials are available in Table S1.

The possibility to tune the loadings of the encapsulated enzyme and mediator in ABTS/HRP@ZIF-8 was explored. For the preparation of ABTS/HRP@ZIF-8 materials with different loadings, the initial concentrations of the redox species were varied while the other synthesis parameters remained constant. For the first method explored, Method A, we obtained the

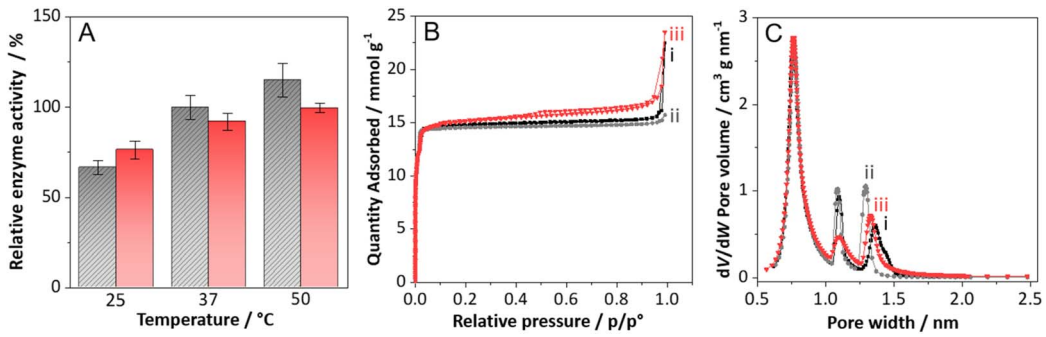

Fig. 2 (A) Relative biocatalytic activity for H_2O_2 conversion based on UV-vis assay with ABTS for (grey, stripes) free HRP *versus* (red, solid) ABTS/HRP@ZIF-8 at 80 μmol L^{-1} H_2O_2 in 50 mmol L^{-1} PB pH 7. (B) Nitrogen adsorption/desorption isotherms and (C) corresponding Horvath–Kawazoe microporous pore size distributions for (i, black) ZIF-8, (ii, grey) HRP@ZIF-8, and (iii, red) ABTS/HRP@ZIF-8.

material $ABTS^{LO}/HRP^{HI}$, where the designations LO and HI correspond to "low" and "high" loading amounts of ABTS (*ca.* 0.5 mg) and HRP (*ca.* 4.2 mg), respectively. For Method A, the enzyme was encapsulated with a very high efficiency of 98% while the redox mediator was encapsulated with an efficiency of 6%. We subsequently explored the possibility to increase ABTS loadings with a view to increasing electron shuttling pathways for bioelectrocatalysis. For Method B, the initial HRP amount employed was similar albeit slightly higher (5.0 mg *vs.* 4.2 mg) while the ABTS amount was increased by a factor of 6 (from 8.3 mg to 50.0 mg). The loading efficiency doubled to 13 ± 1% for ABTS, while the enzyme loading efficiency decreased to only 18 ± 5%, resulting in the composite $ABTS^{HI}/HRP^{LO}$. The use of a high initial amount of ABTS, and therefore a high initial mediator:enzyme ratio, appears to restrict enzyme encapsulation efficiency in the multiple redox MOF mediator/enzyme@ZIF-8 materials. We finally explored Method C, for which a high ABTS amount of 50.0 mg was maintained while the initial enzyme amount was increased from 5.0 mg to 15.0 mg. The enzyme loading amount dramatically increased from 0.9 ± 0.3 mg to *ca.* 3.9 mg, owing to the high initial enzyme amount as well as an improved loading efficiency of *ca.* 26%. Meanwhile, the ABTS loading amount and efficiency of 6.5 mg and 13% was practically unaffected. To maximise the redox loadings of both the redox mediator and enzyme, these results indicate the importance of a low mediator:enzyme ratio when increasing the initial amounts used for synthesis. A series of control materials were also synthesised in an equivalent manner; namely, ABTS@ZIF-8 and HRP@ZIF-8 (loading amounts and efficiencies available in Table S1). The ABTS encapsulation amount and efficiency for ABTS@ZIF-8 were similar to that of $ABTS^{HI}/HRP^{LO}$@ZIF-8 when the same initial ABTS concentration was used. In contrast, for HRP@ZIF-8, a far higher loading efficiency of 75 ± 6% was observed *vs.* the *ca.* 26% loading efficiency for $ABTS^{HI}/HRP^{LO}$@ZIF-8. At least for the $ABTS^{HI}/HRP^{LO}$@ZIF-8 material, the presence of ABTS had a more disruptive effective on enzyme encapsulation than *vice versa*. We emphasise that, unless stated otherwise, the ABTS/HRP@ZIF-8 material described throughout this study corresponds to the $ABTS^{HI}/HRP^{LO}$@ZIF-8 material obtained using Method B, a material that offers a compromise in terms of loading and economic considerations.

Design and screening of redox-active (bio)mineralised ZIF-8 for bioelectrocatalysis at carbon nanotube electrodes

The redox-active (bio)mineralised MOFs were explored as adsorbed layers on multiwalled CNT-modified glassy carbon electrodes for the two-electron two-proton bioelectrocatalytic reduction of H_2O_2 to H_2O. It is well-known that HRP is able to undergo H_2O_2 electro-reduction *via* mediated as well as direct electron transfer processes, hence both of these strategies were explored[17,24,25,27,50] CNT electrodes are attractive for bioelectrocatalysis owing to properties such as their hierarchical nanostructured porosity, high surface area, high conductivity, easy surface modification by adsorption of proteins and (poly) aromatics, and wide electrochemical potential window.[24,62] Here we employed cyclic voltammetry to characterise the electroactivity and bioelectrocatalytic activity of the modified bioelectrodes. Fixed potential chronoamperometry was employed to investigate bioelectrocatalytic substrate inhibition, electrochemical biosensor performance, and storage stability. Table S2 provides a summary of the basic electrochemical parameters determined in simple 50 mmol L^{-1} PB pH 7 at HRP-modified CNT bioelectrodes prepared with ABTS and redox MOF (ABTS@ZIF-8 and ABTS/HRP@ZIF-8) layers: peak potential ($E_{1/2}$), peak-to-peak separation (ΔE_p) and surface concentration (Γ_{ABTS}). Fig. 1B shows a high-resolution SEM image of a representative CNT-ABTS/HRP@ZIF-8 bioelectrode prepared with an adsorbed ABTS/HRP@ZIF-8 layer on the porous CNT substrate. The MOF nanoparticles are distributed relatively uniformly across the CNT network.

Fig. 3 shows cyclic voltammograms (CVs) recorded at diverse redox-active ZIF-8 HRP bioelectrodes to explore their bioelectrocatalytic activity for H_2O_2 reduction. CVs were recorded at 10 mV s^{-1} in the absence then presence of 3 mmol L^{-1} H_2O_2 in 50 mmol L^{-1} phosphate buffer at pH 7. First, we explored HRP@ZIF-8 at CNTs to test the possibility of achieving DET-type bioelectrocatalysis. As shown in Fig. 3A, no bioelectrocatalytic current was observed. The HRP in the insulating and crystalline ZIF-8 structure is electrically-inaccessible. This result is consistent with (i) the electrode-heme site electron transfer distance not being within 20 Å, in line with Marcus theory, and/or (ii) limited mobility (*e.g.* the enzyme is "immobile") restricting favorable enzyme orientation with respect to the CNT electrode.[43,63,64]

We next explored an MET-type configuration in which the CNT electrode was first modified with ABTS molecules prior to immobilisation of HRP@ZIF-8. The adsorption of aromatic

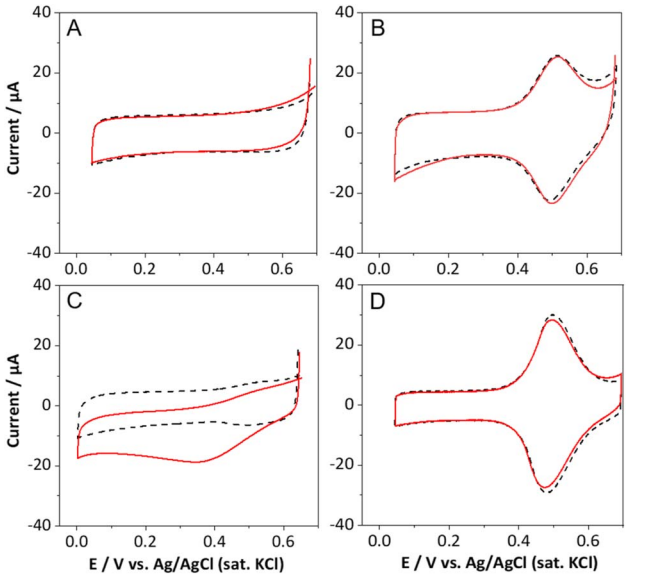

Fig. 3 CVs recorded at 10 mV s^{-1} in 50 mmol L^{-1} PB pH 7 at 37 °C with (black, dash) no H_2O_2 and (red, solid) 3 mmol L^{-1} H_2O_2 for (A) CNT with HRP@ZIF-8, (B) CNT-ABTS with HRP@ZIF-8, (C) CNT with $ABTS^{LO}/HRP^{HI}$@ZIF-8, and (D) CNT with ABTS@ZIF-8 and HRP.

redox mediators at sp^2 carbon electrodes, facilitated by strong π-stacking interactions, is a valuable tool to achieve MET bioelectrocatalysis *e.g.* for biosensing.[4,29,65] As shown in Fig. 3B, both in the absence and presence of H_2O_2, the classical quasi-reversible one-electron electroactivity of adsorbed ABTS molecules is observed at $E_{1/2} = 0.50 \pm 0.02$ V *vs.* Ag/AgCl (sat. KCl).[50,66] Despite a high electroactive surface coverage for the redox mediator of $6.03 \pm 0.12 \times 10^{-9}$ mol cm^{-2}, and fast apparent electron transfer kinetics ($\Delta E_p = 22 \pm 2$ mV at 10 mV s^{-1}), no significant catalytic current was observed after addition of 3 mmol L^{-1} H_2O_2 across a wide potential range. This finding is consistent with efficient electron transfer between the mediator and the electrode but, importantly, no mediated electron transfer between the enzyme and the electrode. This is again consistent with the HRP being buried within an insulating crystalline MOF scaffold, as opposed to the enzyme being present and exposed at the surface for easy electrical access to the mediator and CNTs. The absence of DET may also be due to ineffective orientation of enzymes exposed close to the ZIF-8 surface.

The inability to achieve DET or MET bioelectrocatalysis with the HRP@ZIF-8 layer led us to the development of the redox-active enzyme/mediator@ZIF-8 materials. We first prepared a bioelectrode with the ABTS^{LO}/HRP^{HI}@ZIF-8 material (Method A) to explore the proof-of-concept. In the absence of H_2O_2, the CV at the CNT–ABTS^{LO}/HRP^{HI}@ZIF-8 bioelectrode exhibited the quasi-reversible electroactivity of adsorbed ABTS (Fig. 3C) with very similar $E_{1/2}$ and ΔE_p values compared to the classically adsorbed ABTS configuration (Fig. 2C and Table S2), considering the experimental uncertainty. The CNT–ABTS^{LO}/HRP^{HI}@ZIF-8 bioelectrode only exhibited a surface coverage of electroactive ABTS molecules of $0.16 \pm 0.10 \times 10^{-9}$ mol cm^{-2}. Nevertheless, the ABTS redox functionalities were present and electrically accessible at the ZIF-8 layer. Their electrochemical accessibility with minimal resistance to the heterogeneous electron transfer process ($\Delta E_p = 25 \pm 2$ mV) is consistent with them being easily accessible, with ABTS molecules at or close to the surface of the ZIF-8 structure. In the presence of H_2O_2, a well-defined cathodic current wave with a high onset potential is observed in line with the initial generation of $ABTS_{red}$ (Fig. 3C) and with a concomitant diminution of the $ABTS_{ox}$ peak. This behavior is attributed to mediated bioelectrocatalysis *via* the ABTS^{LO}/HRP^{HI}@ZIF-8 redox MOF layer. We note that the bioelectrocatalytic current relies on the generation of $ABTS_{red}$ for electron shuttling between the enzyme and the CNT electrode during the enzyme reaction, and that the magnitude of the catalytic current is proportional to the turnover rate. The $ABTS_{red}$ acts as a co-substrate in the mechanism. The catalytic wave is well defined and reaches a peak current of −18.76 μA at 0.35 V *vs.* Ag/AgCl (sat. KCl), characteristic of high substrate turnover with substrate depletion near the electrode surface. To our knowledge, this is the first clear evidence for a classical bioelectrocatalytic reaction with a biomineralised MOF, made possible through the intimate inclusion of both the redox mediator and enzyme. The mechanism of redox mediation is complex to unravel, especially considering our limited understanding of the location and orientation of the enzymes, and distances between mediators and enzymes, at the MOF-electrode interaction. One possibility is that the encapsulated ABTS exhibits some diffusional mobility. A second mechanism is considered to be *via* electron hopping and/or collisions *e.g.* as reported for redox-active polymer materials, where electron transfer proceeds by sequential self-exchange between adjacent and closely-spaced redox groups; in our case, electron transfer *via* ABTS redox groups within and between pores of the MOF structure that enable electrical contact between the enzyme and the CNTs.[46,67–69]

A fourth bioelectrode configuration was explored in which ABTS@ZIF-8 was used as a new type of "MOF mediator" electron shuttle for the electrical connection of a classically-adsorbed HRP layer. As shown in Fig. 3D, the ABTS@ZIF-8 bioelectrode exhibits well-defined quasi-reversible electroactivity due to ABTS molecules, similar to that observed for an adsorbed ABTS layer modified with HRP@ZIF-8, albeit with a higher surface coverage (Table S2). While the ABTS is electrically accessible and exhibits fast apparent electron transfer kinetics ($\Delta E_p = 17 \pm 2$ mV), no bioelectrocatalytic current was observed in the presence of 3 mmol L^{-1} H_2O_2 in the buffer solution. This result further underlines the difficulty in achieving an efficient electron transfer for bioelectrocatalysis using mineralised MOFs. Most importantly, the results from the 4 different electrode configurations validate the importance of the dual mediator/enzyme biomineralisation strategy. The inability of the ABTS@ZIF-8 nanoparticle layer to act as a redox mediator is consistent with electron movement *via* diffusional mobility, collisions and/or electron hopping not being sufficiently continuous across or around the MOF particles. This is in contrast to our previously developed redox-active polymeric glyconanoparticles with surface-encapsulated ABTS, that enabled mediated bioelectrocatalysis, benefitting from diffusional transport of both the enzyme and redox mediator, and from self-exchange across and around the redox particles.[51]

Redox-active biomineralised ABTS/HRP@ZIF-8 *versus* ABTS–HRP for bioelectrocatalysis at carbon nanotube electrodes

Catalytic voltammograms under static and hydrodynamic conditions at high (inactivating) peroxide concentration. We next performed cyclic voltammetry experiments to evaluate the electroactivity and bioelectrocatalytic activity of ABTS/HRP@ZIF-8 with respect to an equivalent bioelectrode prepared with classically adsorbed ABTS and HRP. For these studies, we employed the ABTS/HRP@ZIF-8 (ABTS^{HI}/HRP^{LO}@-ZIF-8) material. As well as providing a compromise in terms of enzyme loading and cost, the high local concentration of ABTS was considered attractive with respect to boosting electron shuttling, compared to ABTS^{LO}/HRP^{HI}@ZIF-8. First, CVs were recorded in the absence of H_2O_2 to confirm (i) the adsorbed nature and (ii) stability of the electroactive ABTS molecules of the CNT–ABTS/HRP@ZIF-8 bioelectrode (Fig. S10 and S11). As shown in Fig. S10, the CVs recorded at 10 mV s^{-1} at CNT–ABTS/HRP@ZIF-8 and the CNT–ABTS–HRP control bioelectrode in 50 mmol L^{-1} PB pH 7 show the same general ABTS electroactivity as observed previously for the diverse ABTS and

ABTS@ZIF-8 modified electrodes. Conveniently for comparative purposes, the electroactive surface coverages of ABTS for the ABTS/HRP@ZIF-8 MOF bioelectrode and the control bioelectrode (CNT–ABTS–HRP) are very similar at $\Gamma = 7.29 \pm 0.24 \times 10^{-9}$ and $7.42 \pm 0.31 \times 10^{-9}$ mol cm^{-2}, respectively.

Repeat potential cycling in the buffer solution of the ABTS/HRP@ZIF-8 bioelectrode was performed to provide insight into the physical stability of the modified layer. 87% of the initial electroactivity remained after 100 redox cycles, confirming a good level of material retention and chemical reversibility. For the control electrode prepared with ABTS molecules directly adsorbed at the CNT electrode, 98% of the initial electroactivity remained. The stability in both cases reflects the strong nature of the bonding of ABTS molecules (*e.g. via* π–π stacking) with the CNT sidewalls. The lower stability of the ABTS/HRP@ZIF-8 bioelectrode may be attributed to mediator leaching due to more limited bonding interactions between ABTS and CNTs (*e.g.* steric hindrance from the ZIF structure) and/or some framework collapse. For both types of bioelectrode, the electroactivity is consistent with surface-bound species, as opposed to freely-diffusional species: a linear dependence of the anodic and cathodic currents *vs.* the square root of the scan rate was observed in the range of 1–200 mV s^{-1} ($r^2 \geq 0.993$, Fig. S11). For the ABTS/HRP@ZIF-8 bioelectrode, this corresponds well with the notion that the redox entities are encapsulated and relatively "immobile", at least on the timeframe of these experiments.

The bioelectrocatalytic voltammograms recorded at the ABTS/HRP@ZIF-8 bioelectrode and CNT–ABTS–HRP control bioelectrodes are shown in Fig. 4. The experiments were performed at ambient (RT), physiological (37 °C) and high temperature (50 °C) to provide more insight into the temperature activation/deactivation on the bioelectrocatalytic reaction with the redox MOFs. The ABTS/HRP@ZIF-8 and CNT–ABTS–HRP bioelectrodes were prepared using equivalent modifier concentrations and protocols. For the control bioelectrode, prepared first by modification with ABTS, then HRP, two rather than one modification steps were used. The electrode was prepared in a step-wise fashion and is labelled as such, even if it is not considered as an ideal bilayer but rather a complex hybrid assembly of ABTS and HRP species. Fig. 4A–C shows the CVs recorded under static conditions in the absence of H_2O_2 (black, dashed line) and then in the presence of 3 mmol L^{-1} H_2O_2. Well-defined bioelectrocatalytic currents are observed that follow the general trend of increasing catalytic current with increasing temperature from ambient temperature to 50 °C. It is noted that background-subtracted catalytic currents are reported unless stated otherwise, where the background current was obtained in the absence of peroxide, and experiments were performed at each temperature in triplicate.

At low potential, near maximal catalytic currents at the control electrode increased from 4.8 ± 1.6 μA at room temperature to 10.1 ± 2.2 μA at 37 °C and up to 15.1 ± 2.1 μA at 50 °C. In contrast, for the ABTS/HRP@ZIF-8 bioelectrode at the same low potential, the catalytic currents increased from 9.7 ± 1.1 μA at RT to 17.1 ± 2.4 μA at 37 °C and up to 27.3 ± 3.2 μA at 50 °C. The ABTS/HRP@ZIF-8 bioelectrode system with the confined redox species therefore exhibits a similar temperature dependency but, notably, a significant enhancement in the catalytic current outputs. Across the three temperatures, the average catalytic current improvement was 84%. The bioelectrocatalytic waves are generally similar although there are other notable differences besides the low potential catalytic current boost. For example, at 37 °C and 50 °C (Fig. 4E and F) in particular, a more well-defined and important catalytic current (cathodic) increase at the high potential region from 0.55 V to 0.40 V is observed together with a concomitant diminution of the anodic current of the redox mediator oxidation process. This is consistent with, at least in part, a partial mediated electron transfer process for the ABTS/HRP@ZIF-8 material at CNTs. This evidence for mediated electron transfer is most pronounced for the high temperature experiments.

To shed more light on diffusional transport limitations, a third voltammetric cycle was subsequently recorded under hydrodynamic conditions (500 rpm) for each temperature and electrode type (Fig. 4, pink dash-dot). For both the CNT–ABTS–HRP and ABTS/HRP@ZIF-8 bioelectrodes, the maximum catalytic current outputs were increased due to the increased mass transport to/from the electrode. This confirms diffusion limitations under the normal ambient (static) conditions, irrespective of whether enzyme is simply adsorbed or encapsulated in the MOF. For CNT–ABTS–HRP, the near maximal catalytic currents at 0.1 V *vs.* Ag/AgCl (sat. KCl) increased by 38% at RT, and by as much as 66% at 50 °C. For the ABTS/HRP@ZIF-8 bioelectrode, the catalytic currents increased by 21% at RT and by a maximum of 29% at 50 °C. The ABTS/HRP@ZIF-8 electrode is therefore less sensitive to the increased flux of H_2O_2 and protons experienced under hydrodynamic conditions. This reveals steric hindrance to mass transport due to the ZIF-8 matrix which acts, at least to some extent, as a diffusion-limiting porous membrane. The maximum catalytic current that could be achieved under improved mass transport conditions at 37 °C was 35.1 ± 1.2 μA at ABTS/HRP@ZIF-8, which is still significantly higher than the 25.0 ± 2.5 μA obtained at the ABTS–HRP control bioelectrode without the diffusion-limiting MOF later. Together, these results appear to correspond with reported literature for biocatalytic reactions with biomineralised enzyme@MOF materials that report activity enhancements under deactivating conditions, due to enzyme confinement and stabilisation effects.[38,58,70] The enhanced bioelectrocatalytic currents could be due to a more productive enzyme conformation and/or spatial effects that limit enzyme aggregation or unfolding. For the unique case of ABTS/HRP@ZIF-8, the activity enhancement may also be related to an "active" inhibition shielding effect from the ABTS. In the context of biocatalysis, it has been shown that redox species such as ABTS can protect HRP from suicide inactivation by competing with H_2O_2 during the reaction.[71,72]

Fixed potential amperometric currents under hydrodynamic conditions to investigate H_2O_2 substrate inhibition and electrochemical biosensing. We next investigated the concentration dependence at different temperatures to provide insight into substrate inhibition and MOF protection effects for the bioelectrocatalytic reaction. Fixed potential amperometry at

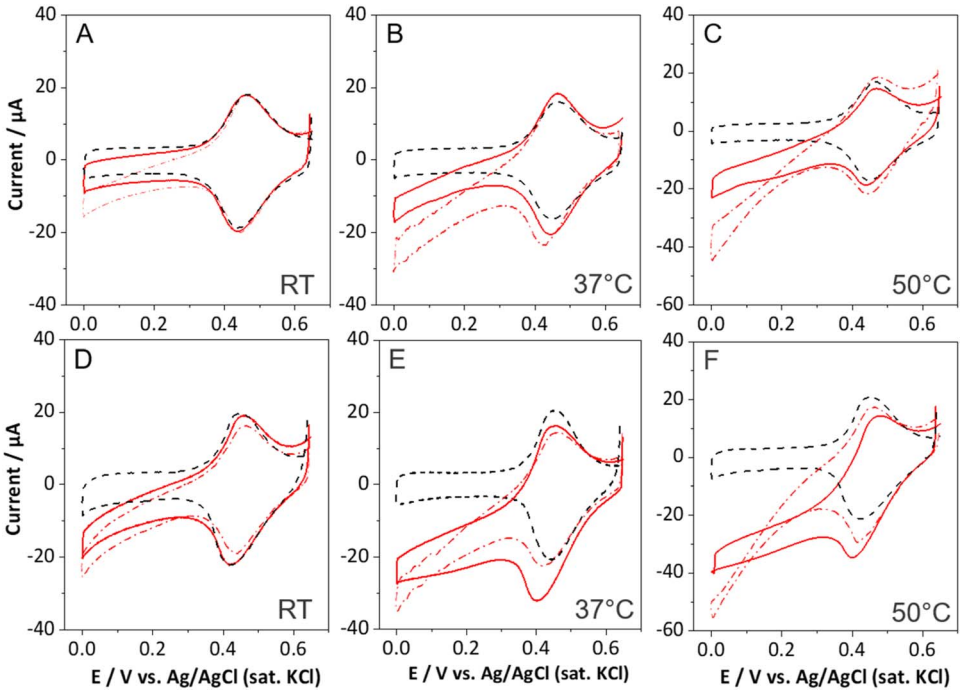

Fig. 4 CVs recorded at 10 mV s^{-1} in 50 mmol L^{-1} PB pH 7 at 37 °C with (black, dash) no H_2O_2, (red, solid) 3 mmol L^{-1} H_2O_2, and (pink, dash-dot) 3 mmol L^{-1} H_2O_2 under hydrodynamic conditions (500 rpm) for (A–C) layer-by-layer CNT–ABTS–HRP at RT, 37 °C and 50 °C, respectively, *versus* (D–F) CNT–ABTS/HRP@ZIF-8 at RT, 37 °C and 50 °C, respectively.

E_{app} = 0.1 V *vs.* Ag/AgCl (sat. KCl) with stirring at 500 rpm was employed to measure catalytic current outputs across a wide H_2O_2 concentration range from 5 μmol L^{-1} up to 5 mmol L^{-1}. Fig. 5A–C reveals the dose-current response curves for the ABTS/HRP@ZIF-8 and ABTS–HRP control bioelectrodes that rise to a maximum as the H_2O_2 concentration increases, then descend towards a zero or non-zero asymptote current as the inhibitor concentration increases further. The reaction profiles that descend to zero or non-zero current correspond to complete and partial substrate inhibition, respectively. For the classical ABTS–HRP bioelectrode without the MOF matrix, we observe high catalytic currents at low (non-inhibiting) concentrations that reach a maximum at H_2O_2 = 0.1 mmol L^{-1}, then drop sharply. In contrast, the ABTS/HRP@ZIF-8 bioelectrodes exhibit smaller catalytic currents at these low H_2O_2 concentrations, importantly, in the absence of substrate inhibition. The lower catalytic currents observed with the ABTS/HRP@ZIF-8 layer are characteristic of the ZIF-8 structure acting as a flux-diffusion membrane, effectively reducing the local concentration of H_2O_2 (and eventually protons), and therefore limiting the catalytic output at the ABTS/HRP@ZIF-8 bioelectrode.

At higher peroxide concentrations, where H_2O_2 = 0.5 mmol L^{-1} (RT, 37 °C) or 0.2 mmol L^{-1} (50 °C), the bioelectrocatalytic currents at the ABTS/HRP@ZIF-8 surpass those observed at the control ABTS–HRP bioelectrode. At these concentrations, the ABTS–HRP bioelectrode is heavily impacted by substrate inhibition. For all temperatures, the catalytic output with ABTS/HRP@ZIF-8 reaches a maximum at H_2O_2 = 1 mmol L^{-1} then decays to a non-zero current value. The ABTS/HRP@ZIF-8 bioelectrode benefits from significant protection against complete substrate inhibition at RT and partial inhibition at higher temperatures. At 1 mmol L^{-1} at 50 °C, the maximum average catalytic current achieved was 27.5 μA, which compared to 9.1 μA at the control bioelectrode, corresponding to a 203% enhancement (triplicate measurements). We note that a supplementary experiment was performed to further demonstrate that the enhanced catalytic performance under strongly inhibiting conditions was intrinsic to the ZIF composite, and not simply due to ineffective distribution and hybridisation of the redox species at the CNT–ABTS–HRP control electrode. Fig. S12 shows that the bioelectrocatalytic currents at 3 mmol L^{-1} H_2O_2 are not enhanced for a control electrode prepared by pre-mixing ABTS and HRP *vs.* the CNT–ABTS–HRP control electrode prepared *via* the classical step-wise mediator then enzyme modification strategy.

To further evaluate substrate inhibition, half-maximal inhibitory concentration values (IC50) were determined from the dose–response curves. The data in Fig. 5A–C was fitted to double-exponential plots with good agreement ($r2 \geq 0.990$) and analysed to determine the relative IC50 values, as shown in Fig. S13. The IC50 values are defined here as the concentration of the substrate needed to inhibit the bioelectrocatalytic response by 50%. Relative as opposed to absolute IC50 values were determined as the half-way point between the experimentally-determined catalytic minimum and maximum values. We report this method as a simple and practical approach for quantifying inhibition that avoids errors associated with the reliability of Michaelis Menten parameters and

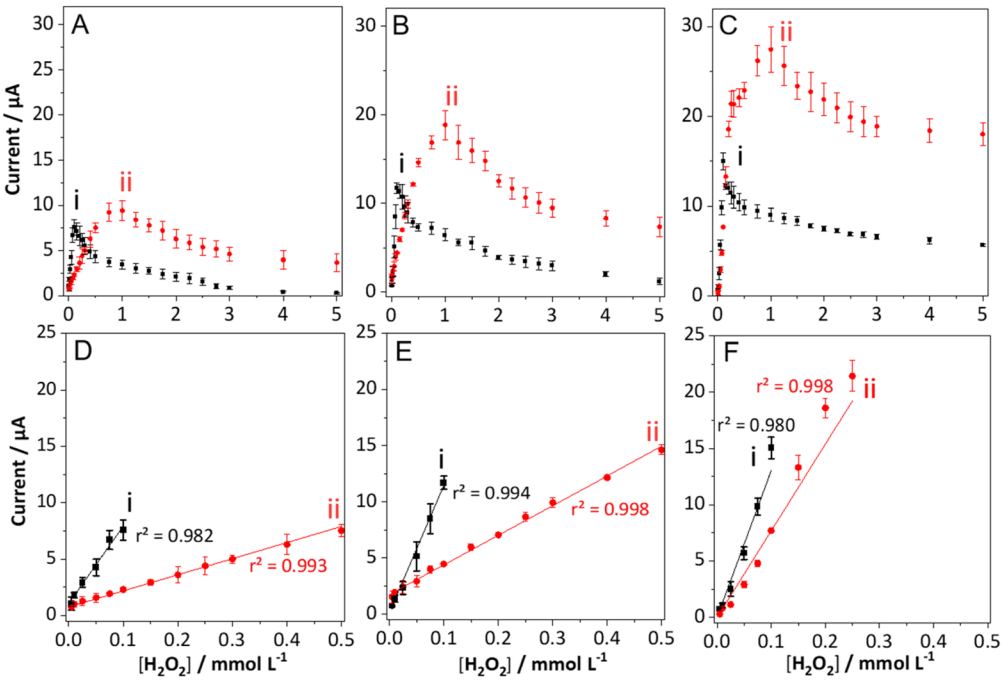

Fig. 5 Fixed potential amperometric current *versus* concentration for (A–C) substrate inhibition and (D–F) linear calibration plots at (i, black) CNT–ABTS–HRP *vs.* (ii, red) CNT–ABTS/HRP@ZIF-8 bioelectrodes. Currents obtained from chronoamperograms recorded at $E_{app} = 0.1$ V *vs.* Ag/AgCl (sat. KCl) in 50 mmol L^{-1} PB pH 7 under hydrodynamic conditions (500 rpm) at (A and D) RT, (B and E) 37 °C, and (C and F) 50 °C.

elucidating the substrate inhibition model.[73] The relative IC50 values for H_2O_2 at the ABTS–HRP bioelectrode ranged from 0.73 ± 0.23 mmol L^{-1} at RT to 0.90 ± 0.06 mmol L^{-1} at 37 °C, to as low as 0.48 ± 0.17 mmol L^{-1} at 50 °C. The lowest IC50 is observed at 50 °C, which reflects the harsh environment of the high temperature. In contrast, the IC50 values for H_2O_2 inhibition at the ABTS/HRP@ZIF-8 bioelectrode ranged from 1.96 ± 0.35 mmol L^{-1} at RT to 1.94 ± 0.16 mmol L^{-1} at 37 °C, and 1.77 ± 0.44 mmol L^{-1} at 50 °C. The biomineralised architecture of ABTS/HRP@ZIF-8 therefore significantly reduces the potency of the peroxide inhibitor across the different temperatures, and especially at 50 °C under harsh thermal conditions. While IC50 values have been reported for diverse HRP inhibitors, reported IC50 values with H_2O_2 as the inhibitor were not identified. For comparison, we estimated an IC50 based on the biocatalytic assay data reported in the study of Nicell and Wright.[74] The estimated IC50 with H_2O_2 as the inhibitor is *ca.* 1.4 mmol L^{-1} at 25 °C at pH 7.4.[74] The estimated literature IC50 is higher than the values we obtained here for the classical ABTS–HRP bioelectrode but lower than the protected ABTS/HRP@ZIF-8 bioelectrode. It's not straightforward to compare owing to the difference in reaction mechanism *e.g.* biocatalytic *vs.* bioelectrocatalytic, which implies different reactivity between immobilised and diffusional enzymes and the different co-substrate/mediators used (*e.g.* phenol *vs.* ABTS), for example.

The ABTS/HRP@ZIF-8 system may also provide some specific advantages for electrochemical biosensing. Fig. 5D–F shows linear calibration curves for H_2O_2 sensing, obtained from the concentration-current plot data in Fig. 5A–C. In this context, the sensitivity and linear dynamic ranges were determined and recorded in Table S3. For the control ABTS–HRP bioelectrodes, the linear detection range was 0.005 to 0.1 mmol L^{-1} across the three temperatures. For the ABTS/HRP@ZIF-8 bioelectrodes, the linear dynamic ranges were 0.005 mmol L^{-1} to either 0.5 mmol L^{-1} (RT, 37 °C) or 0.25 mmol L^{-1} (50 °C). The biomineralisation strategy therefore permits a temperature-dependent 2.5 to 5-fold increase in the upper limit of the linear calibration range for peroxide biosensing. The increase in linear dynamic range is characteristic of the flux-limiting behavior of the ZIF-8 matrix, where the ZIF-8 matrix functions effectively as an alternative membrane to classical polymers such as polycarbonate or nanocellulose.[10,24] The ability to also expand the upper limit of the sensor range beyond 0.1 mmol L^{-1} is promising for environmental, industrial and even biological applications. While H_2O_2 is typically found at relatively low μmol L^{-1} levels *in vivo*, concentrations exceeding 0.1 mmol L^{-1} are found in cellular environments, for example, in the context of cancer therapy monitoring.[75] The HRP/ABTS@ZIF-8 bioelectrode maintains a reasonable level of sensitivity but is nevertheless less sensitive *vs.* the classical layer-by-layer electrode, at least in part due to flux-limiting effects. For example, at 37 °C, the analytical sensitivity for the ABTS–HRP bioelectrode was 400.2 ± 13.8 μA $mmol^{-1}$ cm^{-2}, which compares to 93.4 ± 1.1 μA $mmol^{-1}$ cm^{-2} at the HRP/ABTS@ZIF-8 bioelectrode. The sensitivities are not the highest reported; HRP-based biosensors employing redox-active Os polymers exhibited a higher sensitivity of 297 μA $mmol^{-1}$ cm^{-2}.[76] Elsewhere, mediatorless HRP-modified CNT bioelectrodes exhibited a sensitivity of 5.1 ± 0.2 μA $mmol^{-1}$ cm^{-2}.[77] Overall, the wide linear range and reasonable sensitivity observed here are promising with respect to

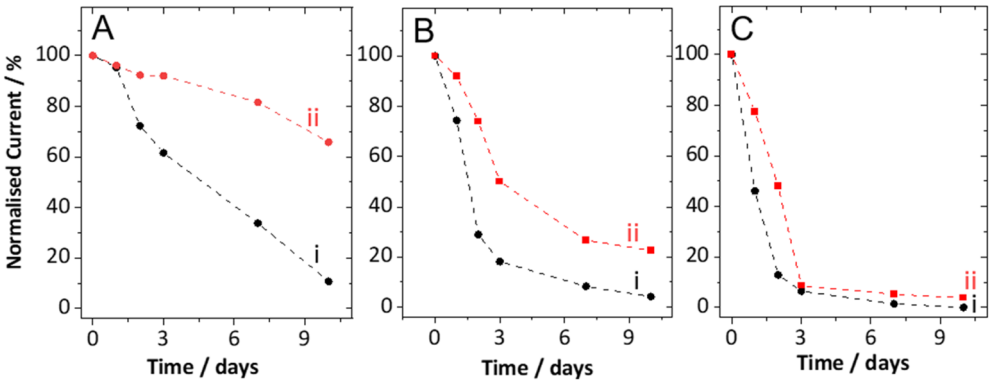

Fig. 6 Relative fixed potential amperometric current *versus* time to assess storage stability over 10 days for (i, black) CNT–ABTS–HRP and (ii, red) CNT–ABTS/HRP@ZIF-8 bioelectrodes. Currents obtained from chronoamperograms recorded for 600 s at $E_{app} = 0.1$ V *vs.* Ag/AgCl (sat. KCl) in 50 mmol L^{-1} PB pH 7 under stirring at 500 rpm at (A) RT, (B) 37 °C, and (C) 50 °C.

biosensing, especially with a view to sensing in strongly dosed or contaminated aqueous matrices, for example.

Initial bioelectrocatalytic stability experiments were performed at the CNT–HRP/ABTS@ZIF-8 and control CNT–ABTS–HRP bioelectrodes to provide preliminary insight into non-substrate inhibition related protection effects. Amperometric currents were periodically recorded on different days at 0.1 V *vs.* Ag/AgCl (sat. KCl) in 50 mmol L^{-1} PB pH 7 with 0.2 mmol L^{-1} H_2O_2 for operational periods of 600 s. The recorded currents were obtained after each operational period of 600 s. The normalized currents were plotted as a function of storage time (days) over a 10-day period, as shown in Fig. 6. First, we can observe that the relative stabilities are consistently higher for the HRP/ABTS@ZIF-8 bioelectrodes across the 10 day period and for all 3 temperatures. This confirms a significant MOF-induced stabilising effect at mild and harsher temperatures. Focusing on the 10-day stability performance, which corresponds to 1800 s of operational testing, only 11%, 4% and <0.1% of the initial catalytic activity remained for the classical ABTS-HRP bioelectrode. The bioelectrodes are clearly unstable, even for tests at mild ambient temperature. For the series at 50 °C, complete deactivation was observed after 10 days in line with a higher level of thermal deactivation. On the other hand, the ABTS/HRP@ZIF-8 bioelectrodes permitted the retention of 66% (RT), 23% (37 °C) and 4% (50 °C) of the initial catalytic activity after 10 days.

While the protection offered by the ABTS/HRP@ZIF-8 material is promising for periodic measurements over several days at RT and physiological temperature, the system is poorly practical for experiments involving temperatures of 50 °C beyond 2 days. We note that a high overpotential of 0.1 V *vs.* Ag/AgCl (sat. KCl) was also used for these experiments and that a more moderate overpotential could help reduce activity degradation. These first storage stability experiments are promising; for example, we previously reported average stabilities of 39% to 67% at RT after 7 days for a HRP/polymer CNT bioelectrode system.[24] The improved storage stabilities are accounted for, at least in part, by flux-limiting effects. The substrate inhibition and thermal inactivation protection may also benefit from chemical and/or physical stabilising interactions between the ZIF and the enzyme that facilitate improved geometry, compactness and/or retention of the protein.

Conclusion

In conclusion, this work demonstrates the ability of biomimetic mineralised zeolitic imidazolate framework MOFs containing an oxidoreductase and a redox mediator to shuttle electrons for a bioelectrocatalytic reduction reaction at carbon nanotubes. Thanks to the intimate inclusion of both the enzyme and a molecular redox mediator during the biomineralisation ZIF-8 synthesis process, electron transfer involving an important density of electron acceptors became possible. Neither direct or mediated electron transfer bioelectrocatalysis could be achieved with a biomineralised crystalline enzyme@ZIF-8 layer at CNTs, or *via* an alternative strategy using a new type of mediator@ZIF-8 material. The synthesis protocols were developed such that the enzyme and mediator loadings could be modulated, to a certain extent. Enhanced bioelectrocatalytic outputs were observed for the enzyme/mediator@ZIF-8 compared to equivalent control systems due to substrate inhibition protection effects. Significant bioelectrocatalytic activity enhancements were observed but only under substrate inhibiting conditions at ≥0.2 mmol L^{-1} H_2O_2 and up to 5 mmol L^{-1}, hence the enhancement mechanism is directly related to inhibition shielding. At 50 °C, the catalytic current enhancement is dramatic, reflecting also thermal deactivation protection effects. Initial stability studies performed over 10 days at low (non-inhibiting) peroxide concentration highlighted beneficial protection effects due to the MOF besides substrate inhibition protection. Together, the results emphasise significant benefits of the biomineralisation strategy, especially under deactivating conditions. This report also introduces bioelectrochemical IC50 for H_2O_2 inhibition that may act as benchmark values for comparisons between peroxidase and other types of inhibited enzymatic electrodes. The practical utility of the ABTS/HRP@ZIF-8 system was demonstrated for proof-of-concept electrochemical biosensing of H_2O_2. A reasonable sensitivity

was observed although sensor sensitivity was negatively impacted compared to a classical layer-by-layer fabricated electrode. On the other hand, an important 2.5 to 5-fold increase in the linear dynamic range of the biosensor was observed, as well as improved 10-day stability over a wide range of temperatures. The biomineralised enzyme/mediator@ZIF-8 system could in principle be used with any other oxidoreductase, with a suitable redox mediator/cofactor, to improve the catalytic activity and stability for diverse bioelectrochemical applications. Based on this study, such redox biomineralised materials are especially adapted for operation under inhibiting and/or deactivating conditions, and are well suited for heavily dosed or contaminated sample analysis rather than trace level detection. Future work is necessary to better understand the spatial arrangement and interactions of the encapsulated enzyme and mediator within the MOF structure (*e.g. via* computational and more advanced spectroscopic methods), and to precisely elucidate the charge transfer process. Besides electrochemical sensors, such MOF-enzyme hybrids should be exploited to benefit biofuel cell and electro-enzymatic reactors where the use of high (deactivating) substrate concentrations and eventually temperatures are desired, or even necessary, for practical use.

Experimental

Chemicals and materials

Sodium phosphate dibasic (Na_2HPO_4, ≥99%), sodium dihydrogen phosphate (NaH_2PO_4, ≥99%), hydrogen peroxide (30% w/w in H_2O), zinc nitrate hexahydrate ($Zn(NO_3)_2 \cdot 6H_2O$, crystallised, ≥99%), 2-methylimidazole (2-MeIm, 99%), 1-methyl-2-pyrrolidone (NMP, ≥99%), and horseradish peroxidase (HRP) from *Armoracia rusticana* were purchased from Sigma Aldrich and used as received without further purification. The enzyme was stored at −4 °C when not in use. 2,2′-azino-bis (3-ethylbenzothiazoline-6-sulfonic acid (ABTS, 98%) was purchased from Thermo Scientific Chemicals. Distilled water (DI water) was purified to a minimum resistivity of 15 MΩ cm^{-1} using a Millipore Ultrapure system. Commercial grade thin multi-walled carbon nanotubes (CNTs, ≥95%) were obtained from Nanocyl and used as received without purification.

Electrochemistry

Cyclic voltammetry experiments were performed using a Biologic VMP3 Multi Potentiostat with EC-lab software. Fixed potential chronoamperometric measurements were performed using a Princeton Applied Research PARSTAT-MC-PMC1000 potentiostat controlled by Versastudio software, operating in a Faraday cage. Hydrodynamic experiments were performed using an IKA C-mag magnetic stirrer at 500 rpm with a magnetic stirrer bar placed in the electrolyte. All experiments were performed with a three-electrode cell comprising a working electrode based on a carbon nanotube film-modified glassy carbon (GC with $Ø = 3$ mm), a silver–silver chloride reference electrode (Ag/AgCl with saturated KCl), and a Pt wire counter electrode. GC electrodes were polished using a Presi polishing cloth with 1 μm alumina then sonicated for 5 min in distilled water prior to use. Electrochemical experiments were performed in 50 mmol L^{-1} phosphate buffer (pH 7). Amperometric data was recorded at $E_{app} = 0.1$ V *vs.* Ag/AgCl (sat. KCl) unless stated otherwise. For the inhibition study, the first peroxide addition was made after 300 s, followed by subsequent additions every 100 s. For stability experiments, bioelectrodes were stored in fresh buffer solution at 4 °C between measurements. The surface concentration of electroactive ABTS, denoted Γ (in mol cm^{-2}) was calculated according to the following equation:

$$\Gamma = Q/nFA \quad (1)$$

where Q is the average charge obtained from the anodic peaks of the redox mediator (in coulombs), n is the number of electrons (1 electron), F is Faraday's constant (96 485 C mol^{-1}), and A is the geometric surface area of the electrode (in cm^2). The charge was calculated as the integral of the peaks associated with the oxidative faradaic process normalised by the scan rate (10 mV s^{-1}).

Synthesis of redox MOFs

ZIF-8. First, 92.5 mg of $Zn(NO_3)_2 \cdot 6H_2O$ was dissolved in 4 mL of DI water. In a second flask, 4.1 g of 2-methylimidazole was dissolved in 40 mL of DI water. The solution of the second flask was added to the first flask $Zn(NO_3)_2 \cdot 6H_2O$. This mixture was left to react under stirring at room temperature (RT). After stirring for 30 min, the product was collected by three centrifugation and DI water rinsing steps (12 000 rpm; 20 min, 4 °C), then the product was dried overnight in an oven at 40 °C.

HRP@ZIF-8. First, 92.5 mg of $Zn(NO_3)_2 \cdot 6H_2O$ was dissolved in 4 mL of DI water. In a second flask, 5.0 mg of HRP was dissolved in 4 mL of DI water, then this volume was added to the first flask. The volume of a third flask containing 4.1 g of 2-MeIm dissolved in 40 mL of DI water was rapidly added to the mixture. The mixture was left to react under stirring at room temperature (RT) for 30 min. After stirring for 30 min, the reaction mixture was aged under static conditions in the fume hood for a further 18 h. The product was collected by three centrifugation and DI water rinsing steps (12 000 rpm; 20 min, 4 °C), then the product was dried overnight in an oven at 40 °C.

ABTS/HRP@ZIF-8. The standard synthesis (Method B) was the same as the protocol for HRP@ZIF-8 except that the volume of a fourth flask containing 50 mg of ABTS in 0.25 mL of DI water was rapidly added after the addition of the 2-MeIm to the mixture of $Zn(NO_3)_2 \cdot 6H_2O$ and HRP. The reaction time and purification was otherwise the same as for HRP@ZIF-8. The alternative syntheses of Method A ($ABTS^{LO}/HRP^{HI}$@ZIF-8) and Method C ($ABTS^{HI}/HRP^{HI}$@ZIF-8) were prepared in the same manner except that the HRP and ABTS amounts were 4.2 mg and 8.3 mg (Method A) and 15 mg and 50 mg (Method C).

ABTS@ZIF-8. The synthesis was performed using the same protocol as for HRP@ZIF-8 except that 50 mg of ABTS in 0.25 mL was rapidly added to the mixture containing 2-MeIm and $Zn(NO_3)_2 \cdot 6H_2O$, as opposed to the addition of the HRP solution. The reaction time and purification was otherwise the same as for HRP@ZIF-8.

Preparation of electrodes

Multiwalled carbon nanotube electrodes. 2.5 mg of the multiwalled carbon nanotubes (CNTs) were first added to 1 mL of NMP in a sealed glass vial and the resulting suspension sonicated for 120 min to achieve a homogeneous dispersion. 20 μL of the CNT dispersion (2.50 mg mL^{-1}) was subsequently drop-casted onto the GC electrode to obtain a densely and homogeneously coated MWCNT layer after drying, based on our previously reported method.[24] The modified electrode was dried under vacuum for 2 h then rinsed with 50 mmol L^{-1} phosphate buffer (pH 7) prior to use.

Modified carbon nanotube bioelectrodes with enzyme, mediator, (bio)mineralised ZIF-8 layers. The control CNT–ABTS–HRP bioelectrodes were prepared from mediator and enzyme solutions prepared at 0.13 mg mL^{-1} and 0.02 mg mL^{-1} in 50 mmol L^{-1} PB pH 7, respectively. First, 20 μL of the ABTS solution was drop-casted on the electrodes and left to react for 60 min at RT. The electrodes were lightly rinsed with the 50 mmol L^{-1} PB pH 7 buffer solution, then immersed in a 20 μL volume of the HRP solution, then left to reactive overnight in the refrigerator (5 °C). The electrodes were lightly rinsed with the buffer solution prior to analysis. The control CNT–ABTS/HRP bioelectrodes were prepared by immersion in a 20 μL of a pre-mixture of ABTS and HRP at 0.13 mg mL^{-1} and 0.02 mg mL^{-1} in 50 mmol L^{-1} PB pH 7. The pre-mixture containing both enzyme and mediator was left to react overnight in the refrigerator (5 °C), then lightly rinsed with the buffer solution prior to analysis.

Unless stated otherwise, the CNT–ABTS/HRP@ZIF-8 modified bioelectrodes were prepared by immersion in a 20 μL volume of the ABTS/HRP@ZIF-8 modifier dispersion prepared at the equivalent concentration as for the individual ABTS and HRP solutions, then left to react at room temperature overnight in the refrigerator (5 °C). The $ABTS^{LO}/HRP^{HI}$@ZIF-8 modifier solution was prepared at 0.02 mg mL^{-1} and 0.18 mg mL^{-1} HRP. The electrodes were lightly rinsed with the buffer solution prior to analysis. The alternative MOF-modified electrodes prepared with additional ABTS or enzyme layers were prepared according to the above immersion protocol for the enzyme solution and MOF dispersions, and drop-casting for the ABTS solutions, with rinsing with buffers solution between each step.

Materials characterisation

UV-vis protocols. Calibration curves for ABTS and HRP were prepared from stock solutions in distilled water and established based on the absorption intensities at $\lambda = 339$ and 402 nm, respectively. The calibration curves were used to estimate the loading amounts in the MOF samples by analysis of the dissolved species in the supernatant solutions and considering the initial enzyme amount used for each synthesis. The enzyme activities of the enzyme and MOF composites were determined according to the classical enzymatic assay of HRP with ABTS and H_2O_2 with continuous spectrophotometric detection of the oxidized light green product, $ABTS^{\cdot+}$, at $\lambda = 402$ nm.[78] The experiments were performed at fixed temperature in 50 mmol L^{-1} PB at pH 7 on a temperature controlled stage. Solutions were warmed to the desired temperature prior to addition into the quartz cuvette in the absence of BSA and Triton X-100.

pXRD. The XRD patterns were collected at room temperature (22 °C) in the Bragg–Brentano geometry using an X'Pert PRO MPD diffractometer (PANalytical (now Malvern Panalytical), Almelo, Netherlands) with a copper anode, using the K_α wavelength ($\lambda = 1.5419$ Å), and a PIXcel 1D Silicon Strip Detector. Samples were prepared for XRD measurement by filling the cavity of a Silicon Zero Background Holder.

BET. Surface area and pore size were obtained from nitrogen sorption measurements using a Micromeritics ASAP2020Plus instrument. Powders were first outgassed at 60 °C for 12 h. N_2 adsorption/desorption isotherms were obtained at 77 K. The specific surface area of the powders was calculated from the N_2 isotherm using the Brunauer–Emmet–Teller (BET) equation in the $0.03 \leq P/P_0 \leq 0.08$ interval of relative pressure and using a cross-sectional area of 16.2 Å for molecular N_2. Micropore size distributions were determined using the Horvath–Kawazoe method.

FT-IR and Raman spectroscopy. Infrared spectra were collected on a Thermo Scientific Nicolet iS10 FT-IR spectrometer equipped with an ATR module for surface analysis. Raman spectra were collected using a WITec alpha300 RA system equipped with a He/Ne laser ($\lambda = 633$ nm) and a Zeiss 50× objective.

SEM. High resolution imaging of was performed using a FEI/Quanta FEG 250 scanning electron microscope (SEM, Hillsboro, OR, USA) with an accelerating voltage of 2.5 kV.

EPR. A Bruker EMX plus spectrometer (Bruker Biospin, Rheinstetten, Germany) equipped with an ESR-900 Helium flow cryostat (Oxford Instruments, Oxfordshire, UK) and an ER 4122SHQE Bruker cavity operating at 9.39 GHz was used. CW X-band EPR spectroscopy was performed on ABTS@ZIF-8, ABTS/HRP@ZIF-8, and the HRP alone in both solid state and in a 10 mmol L^{-1} phosphate buffer at pH = 7. Samples were inserted in an X band quartz sample holder and placed in a He atmosphere. No degassing was attempted.

Author contributions

The manuscript was prepared with contributions from all authors. Conceptualization: M. J., A. J. G.; investigation: M. J., A. U., A. E., S. G., Y. N., T. E., A. J. G.; data curation: M. J. performed MOF synthesis, electrochemistry, UV-vis, FT-IR, and Raman. A. U. performed EPR, A. E. performed MOF synthesis, Y. N. assisted with Raman. T. E. performed XRD; formal analysis: M. J., A. U., S. G., T. E., A. J. G; writing – original draft: M. J., A. J. G.; writing – review and editing: M. J., A. U., A. E., S. G., Y. N., T. E., A. J. G.; funding acquisition: A. J. G.; resources: S. G., A. J. G. Supervision: S. G., A. J. G. All authors have given approval to the final version of the manuscript.

Conflicts of interest

There are no conflicts to declare.

Data availability

The data that support the findings of this study are available in the SI of this article. See DOI: https://doi.org/10.1039/d5ta02717a.

Acknowledgements

This work was funded by the French National Research Agency in the framework of the ANR project CAGEZYMES (grant ANR-20-CE05-0006) that supported the postdoctoral position of M. Joharian. The authors acknowledge the PHC UTIQUE Franco-Tunisian project (CMCU project number: 24G1208) for PhD funding for A. Elloumi. The authors greatly acknowledge the help of Christine Lancelon-Pin (CERMAV Institute, Grenoble) for the SEM images, the work of Valerie Magnin (ISTerre Institute, Grenoble) for BET measurements, and Arielle Le Pellec for invaluable laboratory support throughout the project. We gratefully acknowledge input from Ivan Carrero (voltammetry) and Dr Thomas Lavergne (circular dichroism) at the revisions stage.

References

1 H. Chen, O. Simoska, K. Lim, M. Grattieri, M. Yuan, F. Dong, Y. S. Lee, K. Beaver, S. Weliwatte, E. M. Gaffney and S. D. Minteer, *Chem. Rev.*, 2020, **120**, 12903.
2 J. Pak, W. Chang, C. H. Kwon and J. Cho, *Adv. Funct. Mater.*, 2024, 2415933.
3 Y. Chen, X. Wan, G. Li, J. Ye, J. Gao and D. Wen, *Adv. Funct. Mater.*, 2024, **34**, 2404329.
4 B. Darmau, M. Sacchi, I. Texier-Nogues and A. J. Gross, *Adv. Healthcare Mater.*, 2025, **14**, 2403209.
5 A. Berezovska, P. H. M. Buzzetti, Y. Nedellec, C. Gondran, F. Giroud, A. J. Gross, S. Marinesco and S. Cosnier, *Cell Rep. Phys. Sci.*, 2024, **5**, 102203.
6 H. Wu, Y. Zhang, A.-L. Kjøniksen, X. Zhou and X. Zhou, *Adv. Funct. Mater.*, 2021, **31**, 2103976.
7 T. Saha, R. Del Caño, K. Mahato, E. De la Paz, C. Chen, S. Ding, L. Yin and J. Wang, *Chem. Rev.*, 2023, **123**, 7854.
8 X. Chen, L. Yin, J. Lv, A. J. Gross, M. Le, N. G. Gutierrez, Y. Li, I. Jeerapan, F. Giroud, A. Berezovska, R. K. O'Reilly, S. Xu, S. Cosnier and J. Wang, *Adv. Funct. Mater.*, 2019, **29**, 1905785.
9 S. El Ichi-Ribault, J.-P. Alcaraz, F. Boucher, B. Boutaud, R. Dalmolin, J. Boutonnat, P. Cinquin, A. Zebda and D. K. Martin, *Electrochim. Acta*, 2018, **269**, 360.
10 A. Heller and B. Feldman, *Chem. Rev.*, 2008, **108**, 2482.
11 Abbott, *Abbott's Biowearable: One Sensor for Glucose, Ketones*, 2022, https://www.abbott.com/corpnewsroom/strategy-and-strength/abbotts-biowearable-one-sensor-for-glucose-ketones.html.
12 D. G. Boucher, E. Carroll, Z. A. Nguyen, R. G. Jadhav, O. Simoska, K. Beaver and S. D. Minteer, *Angew. Chem.*, 2023, **135**, e202307780.
13 H. Chen, T. Tang, C. A. Malapit, Y. S. Lee, M. B. Prater, N. S. Weliwatte and S. D. Minteer, *J. Am. Chem. Soc.*, 2022, **144**, 4047.
14 K. Kano, *Biosci. Biotechnol. Biochem.*, 2022, **86**, 141.
15 P. Kokkonen, A. Beier, S. Mazurenko, J. Damborsky, D. Bednar and Z. Prokop, *RSC Chem. Biol.*, 2021, **2**, 645.
16 B. Valderrama, M. Ayala and R. Vazquez-Duhalt, *Chem. Biol.*, 2002, **9**, 555.
17 M. Dequaire-Rochelet, B. Limoges and J. Moiroux, *J. Am. Chem. Soc.*, 2002, **124**, 240.
18 K. Hiraka, W. Tsugawa, R. Asano, M. A. Yokus, K. Ikebukuro, M. A. Daniele and K. Sode, *Biosens. Bioelectron.*, 2021, **176**, 112933.
19 P. N. Bartlett, P. R. Birkin, J. H. Wang, F. Palmisano and G. De Benedetto, *Anal. Chem.*, 1998, **70**, 3685.
20 M. Mallikarjuna and R. Senthamarai, *J. Electroanal. Chem.*, 2023, **946**, 117699.
21 M. Bourourou, K. Elouarzaki, N. Lalaoui, C. Agnès, A. Le Goff, M. Holzinger, A. Maaref and S. Cosnier, *Chem.–Eur. J.*, 2013, **19**, 9371.
22 V. Mishyn, J. Floret, B. Chabbert, V. Aguié-Béghin, D. Crônier, N. G. G. Carducci, D. P. Hickey and S. Abdellaoui, *ChemCatChem*, 2025, **17**, e202401537.
23 P. Bollella and L. Gorton, *Curr. Opin. Electrochem.*, 2018, **10**, 157.
24 S. Bocanegra-Rodríguez, C. Molins-Legua, P. Campíns-Falcó, F. Giroud, A. J. Gross and S. Cosnier, *Biosens. Bioelectron.*, 2021, **187**, 113304.
25 R. Andreu, E. E. Ferapontova, L. Gorton and J. J. Calvente, *J. Phys. Chem. B*, 2007, **111**, 469.
26 C. Abreu, Y. Nedellec, O. Ondel, F. Buret, S. Cosnier, A. Le Goff and M. Holzinger, *J. Power Sources*, 2018, **392**, 176.
27 W. Jia, S. Schwamborn, C. Jin, W. Xia, M. Muhler, W. Schuhmann and L. Stoica, *Phys. Chem. Chem. Phys.*, 2010, **12**, 10088.
28 C. Gomez, S. Shipovskov and E. E. Ferapontova, *J. Renew. Sustain. Energy*, 2010, **2**, 013103.
29 A. J. Gross, X. Chen, F. Giroud, C. Abreu, A. Le Goff, M. Holzinger and S. Cosnier, *ACS Catal.*, 2017, **7**, 4408.
30 B. Valderrama, *Biocatalysis Based on Heme Peroxidases*, ISBN 978-3-642-12626-0. Springer-Verlag Berlin Heidelberg, 2010, pp. 291–2010.
31 B. Limoges, J.-M. Savéant and D. Yazidi, *J. Am. Chem. Soc.*, 2003, **125**, 9192.
32 K. Nazari, A. Mahmoudi, M. Shahrooz, R. Khodafarin and A. A. Moosavi-Movahedi, *J. Enzyme Inhib. Med. Chem.*, 2005, **20**, 285.
33 K. Jayakumar, A. Lielpetere, D. A. Domingo-Lopez, R. E. Levey, G. P. Duffy, W. Schuhmann and D. Leech, *Biosens. Bioelectron.*, 2023, **219**, 114815.
34 M. M. Hossain, M. Rezki, I. Shalayel, A. Zebda and S. Tsujimura, *ACS Appl. Mater. Interfaces*, 2024, **16**, 44004.
35 H. Li, D. Buesen, S. Dementin, C. Léger, V. Fourmond and N. Plumeré, *J. Am. Chem. Soc.*, 2019, **141**, 16734.
36 S. Hardt, S. Stapf, D. T. Filmon, J. A. Birrell, O. Rüdiger, V. Fourmond, C. Léger and N. Plumeré, *Nat. Catal.*, 2021, **4**, 251.
37 A. Rodriguez-Abetxuko, E. Romero-Ben, A. Ontoria, M. Heredero, B. Martín-García, K. Kumar, S. Martín-

Saldaña, F. Conzuelo and A. Beloqui, *Adv. Funct. Mater.*, 2024, **34**, 2400479.
38 K. Liang, R. Ricco, C. M. Doherty, M. J. Styles, S. Bell, N. Kirby, S. Mudie, D. Haylock, A. J. Hill, C. J. Doonan and P. Falcaro, *Nat. Commun.*, 2015, **6**, 7240.
39 T. Sheng, X. Guan, C. Liu and Y. Su, *ACS Appl. Mater. Interfaces*, 2021, **13**, 52234.
40 F.-S. Liao, W.-S. Lo, Y.-S. Hsu, C.-C. Wu, S.-C. Wang, F.-K. Shieh, J. V. Morabito and L.-Y. Chou, *J. Am. Chem. Soc.*, 2017, **139**, 6530.
41 G. Chen, X. Kou, S. Huang, L. Tong, Y. Shen, W. Zhu, F. Zhu and G. Ouyang, *Angew. Chem., Int. Ed.*, 2020, **59**, 2867.
42 G. Chen, S. Huang, X. Kou, S. Wei, S. Huang, S. Jiang, J. Shen, F. Zhu and G. Ouyang, *Angew. Chem., Int. Ed.*, 2019, **58**, 1463.
43 P. N. Bartlett and F. A. Al-Lolage, *J. Electroanal. Chem.*, 2018, **819**, 26.
44 B. Auer, S. G. Telfer and A. J. Gross, *Electroanalysis*, 2023, **35**, e202200145.
45 W. Chen, W. Yang, Y. Lu, W. Zhu and X. Chen, *Anal. Methods*, 2017, **9**, 3213.
46 M. Rezki, M. M. Hossain, T. K. Savage, Y. Tokunou and S. Tsujimura, *Mater. Horiz.*, 2024, **12**, 760.
47 M. Kinoshita, S. Yanagida, T. Gessei and A. Monkawa, *J. Cryst. Growth*, 2022, **600**, 126877.
48 K. Kida, M. Okita, K. Fujita, S. Tanaka and Y. Miyake, *CrystEngComm*, 2013, **15**, 1794.
49 L. Tong, S. Huang, Y. Shen, S. Liu, X. Ma, F. Zhu, G. Chen and G. Ouyang, *Nat. Commun.*, 2022, **13**, 951.
50 I. Jeerapan, Y. Nedellec and S. Cosnier, *Nanomaterials*, 2024, **14**, 545.
51 A. J. Gross, X. Chen, F. Giroud, C. Travelet, R. Borsali and S. Cosnier, *J. Am. Chem. Soc.*, 2017, **139**, 16076.
52 J. Cui, Y. Feng, T. Lin, Z. Tan, C. Zhong and S. Jia, *ACS Appl. Mater. Interfaces*, 2017, **9**, 10587.
53 X. Wu, H. Yue, Y. Zhang, X. Gao, X. Li, L. Wang, Y. Cao, M. Hou, H. An, L. Zhang, S. Li, J. Ma, H. Lin, Y. Fu, H. Gu, W. Lou, W. Wei, R. N. Zare and J. Ge, *Nat. Commun.*, 2019, **10**, 5165.
54 A. F. Ogata, A. M. Rakowski, B. P. Carpenter, D. A. Fishman, J. G. Merham, P. J. Hurst and J. P. Patterson, *J. Am. Chem. Soc.*, 2020, **142**, 1433.
55 M. de J. Velásquez-Hernández, R. Ricco, F. Carraro, F. T. Limpoco, M. Linares-Moreau, E. Leitner, H. Wiltsche, J. Rattenberger, H. Schröttner, P. Frühwirt, E. M. Stadler, G. Gescheidt, H. Amenitsch, C. J. Doonan and P. Falcaro, *CrystEngComm*, 2019, **21**, 4538.
56 M. Ahmad, R. Patel, D. T. Lee, P. Corkery, A. Kraetz, Prerna, S. A. Tenney, D. Nykypanchuk, X. Tong, J. I. Siepmann, M. Tsapatsis and J. A. Boscoboinik, *ACS Appl. Mater. Interfaces*, 2024, **16**, 27887.
57 G. Kumari, K. Jayaramulu, T. K. Maji and C. Narayana, *J. Phys. Chem. A*, 2013, **117**, 11006.
58 K. Liang, C. J. Coghlan, S. G. Bell, C. Doonan and P. Falcaro, *Chem. Commun.*, 2015, **52**, 473.
59 Y. Weng, R. Chen, Y. Hui, D. Chen and C.-X. Zhao, *Chem Bio Eng.*, 2024, **1**, 99.
60 M. M. Maltempo, P. I. Ohlsson, K. G. Paul, L. Petersson and A. Ehrenberg, *Biochemistry*, 1979, **18**, 2935.
61 C. E. Schulz, R. Rutter, J. T. Sage, P. G. Debrunner and L. P. Hager, *Biochemistry*, 1984, **23**, 4743.
62 A. J. Gross, S. Tanaka, C. Colomies, F. Giroud, Y. Nishina, S. Cosnier, S. Tsujimura and M. Holzinger, *ChemElectroChem*, 2020, **7**, 4543.
63 Z. Armstrong, A. MacRae, M. Lenertz, Q. Li, K. Johnson, A. Scheiwiller, P. Shen, L. Feng, M. Quadir and Z. Yang, *ACS Appl. Mater. Interfaces*, 2023, **15**, 38124.
64 R. D. Milton and S. D. Minteer, *J. R. Soc. Interface.*, 2017, **14**, 20170253.
65 M. Holzinger, S. Cosnier and P. H. M. Buzzetti, *Synth. Met.*, 2023, **292**, 117219.
66 K. Elouarzaki, M. Bourourou, M. Holzinger, A. L. Goff, R. S. Marks and S. Cosnier, *Energy Environ. Sci.*, 2015, **8**, 2069.
67 A. Heller, *Curr. Opin. Chem. Biol.*, 2006, **10**, 664.
68 S. Lin, P. M. Usov and A. J. Morris, *Chem. Commun.*, 2018, **54**, 6965.
69 K. Habermüller, M. Mosbach and W. Schuhmann, *Fresenius. J. Anal. Chem.*, 2000, **366**, 560.
70 J. Liang, M. Y. Bin Zulkifli, J. Yong, Z. Du, Z. Ao, A. Rawal, J. A. Scott, J. R. Harmer, J. Wang and K. Liang, *J. Am. Chem. Soc.*, 2022, **144**, 17865.
71 M. B. Arnao, M. Acosta, J. A. del Rio and F. García-Cánovas, *Biochim. Biophys. Acta*, 1990, **1038**, 85.
72 D. Morales-Urrea, A. López-Córdoba and E. M. Contreras, *Sci. Rep.*, 2023, **13**, 13363.
73 S. Abdellaoui, A. Noiriel, R. Henkens, C. Bonaventura, L. J. Blum and B. Doumèche, *Anal. Chem.*, 2013, **85**, 3690.
74 J. A. Nicell and H. Wright, *Enzyme Microb. Technol.*, 1997, **21**, 302.
75 T. Ali, D. Li, T. N. F. Ponnamperumage, A. K. Peterson, J. Pandey, K. Fatima, J. Brzezinski, J. A. R. Jakusz, H. Gao, G. E. Koelsch, D. S. Murugan and X. Peng, *Cancers*, 2024, **16**, 2171.
76 P. Bollella, L. Medici, M. Tessema, A. A. Poloznikov, D. M. Hushpulian, V. I. Tishkov, R. Andreu, D. Leech, N. Megersa, M. Marcaccio, L. Gorton and R. Antiochia, *Solid State Ionics*, 2018, **314**, 178.
77 F. Chekin, L. Gorton and I. Tapsobea, *Anal. Bioanal. Chem.*, 2015, **407**, 439.
78 S. Aldrich, *Enzymatic Assay of Peroxidase*, **https://www.sigmaaldrich.com/deepweb/assets/sigmaaldrich/product/documents/260/895/p6782enz.pdf**, 1996, accessed: March 2025.